Plasma Sources
Science and
Technology

PAPER • **OPEN ACCESS**

Measurements and kinetic modeling of O_2 vibrational kinetics in O_2–Ar mixtures partially dissociated by a Ns pulse discharge

To cite this article: Keegan Orr *et al* 2025 *Plasma Sources Sci. Technol.* **34** 015002

OPEN ACCESS
IOP Publishing
Plasma Sources Science and Technology
Plasma Sources Sci. Technol. **34** (2025) 015002 (20pp)
https://doi.org/10.1088/1361-6595/ad93ff

Measurements and kinetic modeling of O_2 vibrational kinetics in O_2–Ar mixtures partially dissociated by a Ns pulse discharge

Keegan Orr[1,*], Fabrizio Esposito[2], Iole Armenise[2], Dirk van den Bekerom[3] and I V Adamovich[1]

[1] Department of Mechanical and Aerospace Engineering, Ohio State University, Columbus, OH 43210, United States of America
[2] CNR ISTP (Consiglio Nazionale delle Ricerche Istituto per la Scienza e Tecnologia dei Plasmi), Sede Secondaria di Bari, Via Amendola 122/D, 70126 Bari, Italy
[3] Netherlands Organization for Applied Scientific Research (TNO), Urmonderbaan 22, 6167 RD Geleen, The Netherlands

E-mail: keegorr94@gmail.com

Received 29 August 2024, revised 7 November 2024
Accepted for publication 18 November 2024
Published 21 January 2025

Abstract

Vibrational kinetics of O_2 is studied during the O atom recombination in an O_2–Ar mixture, partially dissociated by a burst of ns discharge pulses in a heated plasma flow reactor. The time-resolved temperature in the discharge afterglow is determined by Rayleigh scattering. Time-resolved O atom number density is measured by ps Two-Photon absorption Laser Induced Fluorescence, calibrated in xenon. Time-resolved vibrational level populations of molecular oxygen, $O_2(v = 8–20)$, are measured by ps Laser Induced Fluorescence (LIF), with the absolute calibration by NO LIF. Time-resolved ozone number density is monitored by broadband UV absorption. The results are compared with the predictions of a state-specific kinetic model. The experimental data indicate a rapid initial decay of $O_2(v)$ populations generated by electron impact in the discharge, due to the vibration-translation (V–T) relaxation by O atoms. This is followed by a slower population reduction, on the time scale much longer compared to that for V–T relaxation or vibration-vibration (V–V) exchange. Both O atoms and the $O_2(v)$ populations decay on the same time scale, indicating that chemical reactions initiated by the O atom recombination result in the generation of vibrationally excited O_2 molecules. These trends are reproduced by the kinetic model, which shows that the reaction of O atoms with ozone is the dominant pathway of $O_2(v)$ generation at the present conditions. The predicted relative $O_2(v)$ populations are close to the experimental results, but absolute number densities differ from the experimental data. This is likely due to uncertainties in the absolute calibration of LIF measurements and in the spectroscopic model used in the data reduction. The present work

* Author to whom any correspondence should be addressed.

demonstrates the capability for the absolute, time-resolved measurements of vibrationally excited O_2 in recombining gas flows, to quantify the energy partition in the recombination reactions.

Supplementary material for this article is available online

Keywords: plasma, vibrational kinetics, oxygen, ozone, LIF, TALIF, modeling

1. Introduction

The critical role of vibrational excitation of molecular oxygen during its dissociation in nonequilibrium high-enthalpy flows and in nonequilibrium plasmas has been recognized for a long time [1], and has been reexamined recently in shock tube experiments [2–4]. Kinetics of vibrationally excited states of O_2 generated during the reverse reaction, recombination of O atoms, has also attracted considerable attention [5–9], due to their significant effect on the surface heat flux in partially dissociated flows in the high-temperature boundary layer. The energy fraction of recombining species going into the vibrational excitation of the products is of critical importance, since it directly affects the chemical reaction energy thermalized locally as heat, which controls the wall heat flux. Although significant O_2 vibrational populations and O atom number density can be generated in shock tubes [2–4] and inductively coupled plasmas [10–12], the accurate experimental quantification of this effect in these environments is difficult. In spite of the remarkable recent progress in laser diagnostics, paving the way to the low-uncertainty measurements of O_2 vibrational level populations and nonequilibrium dissociation factor in shock tubes [3, 4], time-resolved state-specific reaction measurements remain extremely challenging.

In the present work, we use a different approach, where the vibrational levels of molecular oxygen in the ground electronic state, $O_2(X^3\Sigma_g^-,v)$, populated during the recombination of O atoms, are monitored in an O_2–Ar mixture partially dissociated by a ns pulse discharge burst in a flow reactor. Comparison of the experimental data with the predictions of a state-specific kinetic model, incorporating nonequilibrium chemical reactions, as well as vibrational–translational (V–T) and vibrational–vibrational (V–V) relaxation, is used to obtain insights into the kinetics of the highly excited vibrational states of O_2. This approach can be used if the reactants (O atoms) are generated in significant amounts at well-characterized conditions, and if the number densities of the reactants and the products (e.g. O atoms and $O_2(X,v)$ molecules, respectively), as well as the gas temperature, are measured at the same time. In the present experiments, oxygen atoms are produced in a repetitive ns pulse discharge in an O_2–Ar mixture, which generates a diffuse, spatially uniform plasma at high pressures and high reduced electric fields [13, 14]. This is critical for efficient O_2 dissociation by electron impact, and by quenching of excited electronic states of Ar atoms. O atom recombination is monitored on a long time scale after the discharge burst, up to of several milliseconds, much longer compared to the time scales for O_2 vibrational relaxation and collisional quenching of excited electronic states of O_2, O, and Ar generated in the discharge. At these conditions, oxygen recombination is dominated by the reactions of O atoms in the ground electronic state, as well as the reactions involving ozone. Although the present measurements are done at relatively low temperatures T = 400–800 K, this approach can be also extended to higher temperatures, up to $T \sim 1500$ K. Since the temperature dependence of the recombination rates is relatively weak, the results can be used for the assessment of the kinetic modeling predictions over a wide temperature range.

2. Experimental

The experimental apparatus used in the present work is shown schematically in figure 1. The heated plasma reactor is a 22 mm × 10 mm rectangular cross section quartz channel fused to the circular quartz tubes, and attached to the quartz endpieces with the fused silica optical access windows. The channel is placed in a tube furnace (Thermcraft XST-4-0-12-1v2-F01), to control the flow preheating temperature. A 20% O_2–Ar mixture flows through the cell at the flow rate of 1 SLM. Heating the flow accelerates the decomposition of ozone, formed in the reactor during the O atom recombination in the flow dissociated by the electric discharge. The flow is excited in a diffuse ns pulse discharge between two parallel rectangular plate copper electrodes 60 mm long and 14 mm wide, mounted to the top and bottom walls in the middle of the quartz channel, as shown in figure 1. The discharge is sustained by a negative polarity MegaImpulse NPG-18/100 kN high-voltage pulse generator (peak voltage 20 kV, pulse duration 20 ns FWHM), operated in burst mode, at a pulse repetition rate of 100 kHz, burst duration of 200 pulses, and burst repetition rate of 10 Hz. The voltage pulse waveform is measured by a Tektronix P6015A high voltage probe. The discharge generates O atoms by electron impact and during the quenching of excited metastable Ar atoms, also generated during the discharge pulses. Between the pulses and after the burst, O atoms generated in the plasma recombine to form ozone and the vibrationally excited O_2 molecules, in the following reactions, as discussed in detail in section 3.

Time resolved vibrational populations of molecular oxygen in the ground electronic state, $O_2(X^3\Sigma_g^-,v)$, and the number density of $O(^3P)$ atoms in the recombining O_2-O-Ar flow are measured by ps single-photon Laser Induced Fluorescence

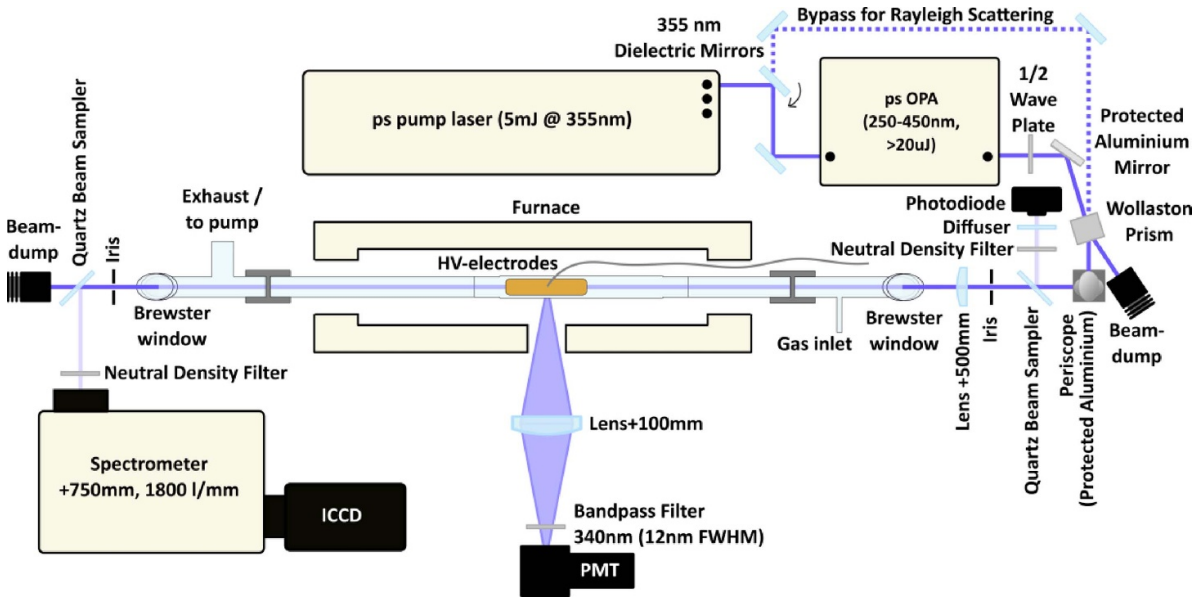

Figure 1. Schematic of the experimental apparatus and optical diagnostics.

(LIF) and ps Two-photon Absorption LIF (TALIF), respectively. This is done using a ps Optical Parametric Oscillator (OPO, Ekspla PG401), pumped by the 3rd harmonic of a 10 Hz ps Nd:YAG laser (Ekspla PL2143A, see figure 1). The OPO produces output at 225–450 nm, with a pulse energy of 15–190 μJ and a linewidth of 2.0–3.5 cm^{-1}, tunable in 0.05–0.1 nm increments. The OPO output linewidth is measured by an Acton SpectraPro HRS-750 0.75 m spectrometer with a 2400 lines/mm grating and a Princeton Instruments ProEM 1600 EMCCD camera, as illustrated in figure 1. The fluorescence signal is detected by a gated photomultiplier (PMT, Hamamatsu R3896) with a narrow bandpass filter (centered near 340 nm with 12 nm FWHM for $O_2(v)$ and centered near 840 nm with 25 nm FWHM for O atom measurements), as shown in figure 1. The ozone number density in the flow excited by the discharge is measured by UV absorption, using a deuterium lamp (Thorlabs SLS204) coupled to an optical fiber and collimating lens. The fiber collimator is placed near the optical access window at the end of the channel, as shown in figure 2. The transmitted light is sent to the same spectrometer as used for the measurements of the OPO line width, for the absorption measurements. The absorption is measured at 250 nm, near the peak of the ozone absorption cross section [15, 16].

The schematics of single-photon LIF transitions used for $O_2(v)$ population measurements, single-photon LIF transitions in NO used for absolute calibration of $O_2(v)$, and the two-photon absorption (TALIF) transitions used for the O atom measurements are shown in figure 3. In figure 3(a), v'' and N'' (J'') are the vibrational and rotational quantum numbers, respectively, of O_2 (NO) probed by the pump transition; v' and N' (J') are the vibrational and rotational quantum numbers, respectively, of O_2 (NO) in the excited electronic states. In all cases, the fluorescence of $O_2(B^3\Sigma_u^-, v' = 0 \rightarrow X^3\Sigma_g^+, v'' = 14)$ is monitored near 337 nm, since this transition has the highest fluorescence yield among the available transitions [17]. The fluorescence transition to $NO(A^2\Sigma^+, v' = 0 \rightarrow X^2\Pi, v'' = 8)$, monitored at nearly the same wavelength, 330–337 nm, is used for calibration. This makes possible the use of NO calibration without changes in the fluorescence signal collection system.

For NO calibration, a room-temperature mixture of NO/N_2 and O_2/Ar with known composition is used. The mixture composition for the calibration is selected such that the fluorescence intensity and lifetime of NO are similar to that of $O_2(v)$. The rates of O_2 predissociation and $NO(A^2\Sigma^+)$ quenching by N_2 and O_2 are taken from [17, 18]. These data are necessary to calculate the O_2 fluorescence yield, which is dominated by the rapid predissociation [17],

$$Y_{O_2} = \frac{A_{O_2}}{A_{O_2} + Q_{pre}}, \tag{1}$$

and the NO fluorescence yield,

$$Y_{NO} = \frac{A_{NO}}{A_{NO} + Q_{NO} + Q_{N_2} + Q_{O_2} + Q_{Ar}}. \tag{2}$$

In equations (1) and (2), A_i are the transition-specific Einstein coefficients for spontaneous emission, Q_{pre} is the predissociation rate, and Q_i are the $NO(A^2\Sigma^+)$ quenching rates by NO, N_2, O_2, and Ar. To relate the absolute populations of O_2 vibrational states to the fluorescence signal during the LIF measurements, we used a synthetic LIF spectrum code, validated vs. LIFBASE [19] for NO, and vs. the code used in [20] for O_2. The OPO output (pump) spectral line shape, used as one of the entry parameters of the code, is determined using a spectrometer, deconvolving the measured line shape and the instrument function. The instrument function is determined by

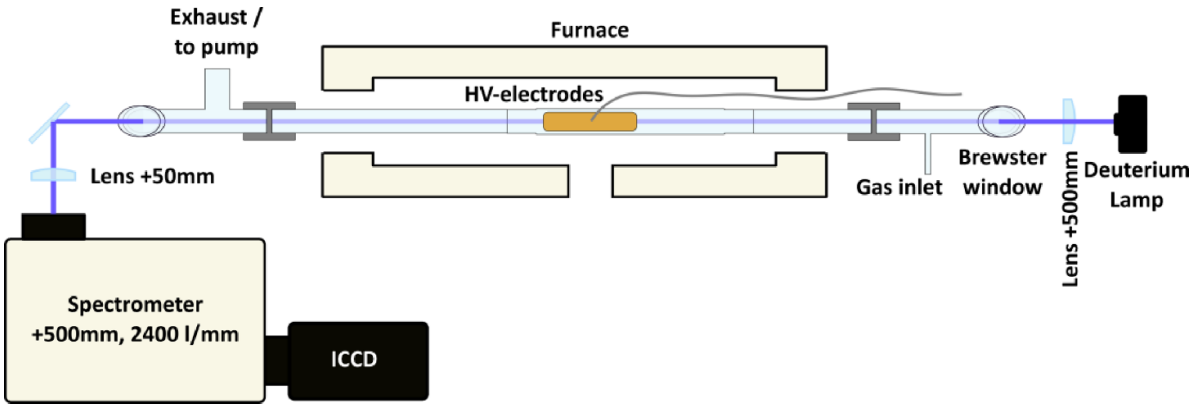

Figure 2. Schematic of ozone measurements by the broadband UV absorption.

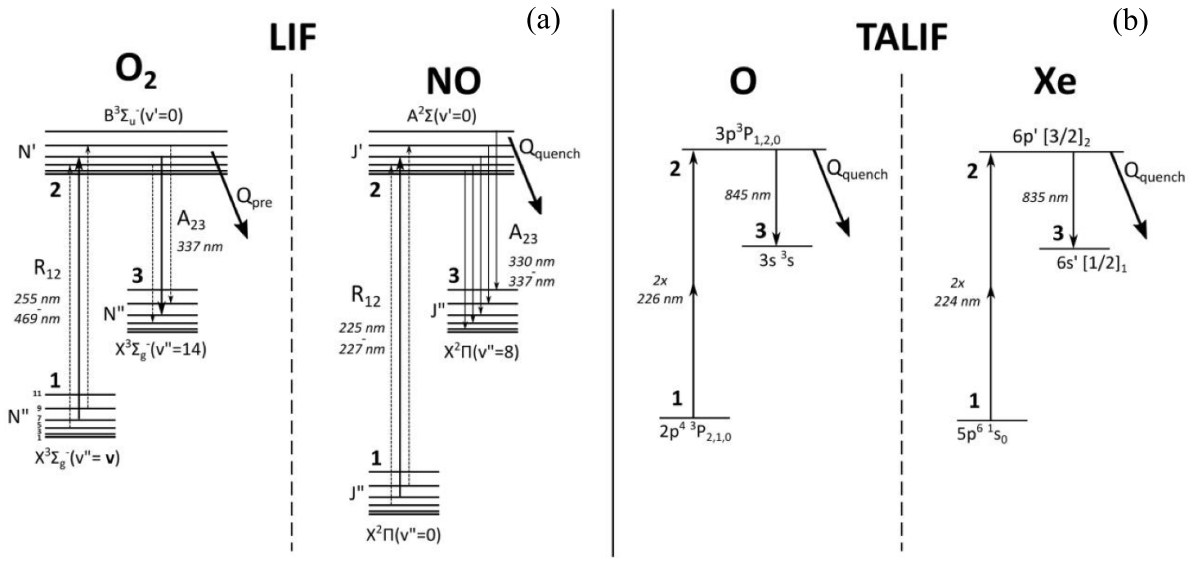

Figure 3. (a) Schematic of O_2 and NO pump and fluorescence transitions used for $O_2(v)$ LIF and NO calibration. R_{12} and A_{23} indicate the pump and fluorescence transitions, respectively; $Q_{\text{pre and}}$ Q_{quench} denote the predissociation and quenching of the upper state of O_2 and NO, respectively. (b) Schematic of O and Xe pump and fluorescence transitions used for O TALIF.

measuring the Hg atomic transition closest to the OPO output wavelength, using a mercury vapor/argon spectroscopic lamp. This was done for each wavelength used for the LIF measurements. For some wavelengths, there is a significant uncertainty in the inferred OPO line shape, since it becomes comparable to the instrument function. There is also an additional uncertainty in the absolute calibration of the spectrometer, for the wavelengths that do not have an adjacent Hg line, such that the calibration line and the OPO output could not be measured without moving the grating of the spectrometer. These effects contribute to the uncertainty of the absolute calibration of the $O_2(v)$ measurements, as discussed below.

O_2 vibrational levels, populated during the recombination reactions, are monitored by LIF on the O_2 Schumann-Runge bands, similar to the approach used in [20]. As stated above, during the LIF measurements, the vibrational level of the upper state was kept the same, $v' = 0$. The decay of the $O_2(A^2\Sigma^+)$ state is dominated by rapid predissociation, which is much faster than collisional quenching [17]. For every O_2 vibrational level probed, the strongest vibrational-rotational lines at the given temperature are selected, using the synthetic fluorescence spectrum. Due to the relatively broad OPO output line width, 2.0–3.5 cm^{-1}, it may also produce excitation on other rotational transitions, as illustrated in figure 4. This is accounted for in the LIF data reduction. Note that the fluorescence from $v'' = 14$ is not accessible in the present LIF scheme, because the OPO excitation wavelength is within the pass band of the bandpass filter. Vibrational levels $v'' = 15$, 16 cannot be accessed since the OPO does not produce the output in this spectral range. Figure 5 compares the synthetic NO LIF excitation spectrum (line) with the experimental NO LIF spectrum (symbols), obtained by the stepwise tuning of the OPO, showing good overall agreement. During the $O_2(v)$ LIF measurements, the OPO output power, monitored by a photodiode with a neutral density filter (see figure 1) was kept in a linear regime. This was verified by measuring the fluorescence signal vs. the OPO power, which scaled linearly.

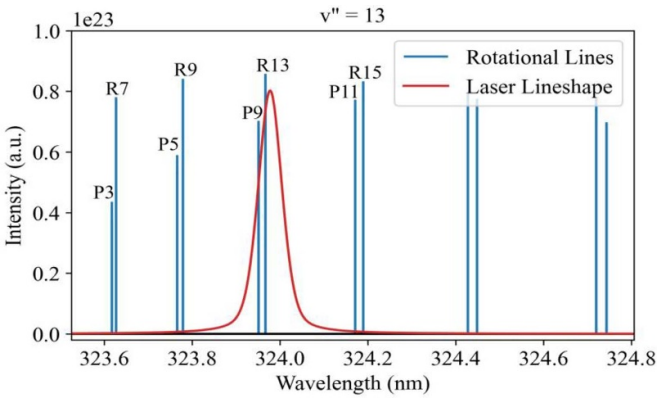

Figure 4. Optical Parametric Oscillator (OPO) line shape and $O_2(B^3\Sigma_u^-, v' = 0, N' \leftarrow X^3\Sigma_g^-, v'' = 13, N'')$ pump transitions at $T = 600$ K. The pump transitions appear as narrow peaks since the absorption linewidth is much smaller compared to that of the OPO, inferred from its spectra.

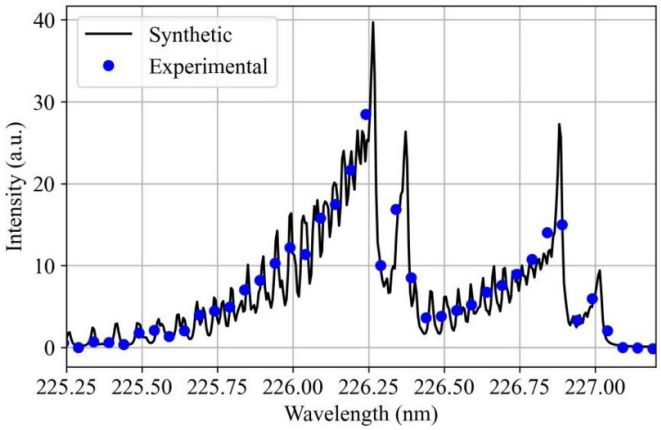

Figure 5. Comparison of the experimental $NO(A^2\Sigma^+, v' = 0, X^2\Pi_r, v'' = 0)$ LIF excitation spectrum, taken in a 67% N_2, 27% Ar, 7% O_2, and 67 ppm NO calibration mixture at room temperature at $P = 150$ Torr, with the synthetic spectrum. Oxygen is added to the mixture to enhance the quenching rate, such that the fluorescence lifetime of NO is similar to that of $O_2(v)$.

The O atom number density in the recombining flow is measured using a two-photon absorption LIF transition at 225.65 nm, which corresponds to the $J'' = 2$ component of the triplet ground electronic state, $O(^3P)$. Fluorescence is detected by the same PMT, using a different bandpass filter, centered near 840 nm with 25 nm FWHM. For absolute calibration, the TALIF signal in the O_2–Ar afterglow is compared to that of xenon excited at 224.35 nm, using the calibration technique described in detail in [21]. During the measurements, the OPO is maintained within the quadratic TALIF signal range. This ensures that the pump intensity remains below the threshold for photoionization and other nonlinear optical effects, which would introduce additional uncertainty in the measurements.

The temperature of the flow excited by the discharge in the cell is measured by Rayleigh scattering thermometry. For this, the 5 mJ 355 nm beam from the pump Nd:YAG laser is used, bypassing the OPO, as shown in figure 1. For these measurements, the PMT on the side of the reactor cell is replaced with a Princeton Instruments PI-MAX 3 ICCD camera to image the scattering of the laser beam through the side wall of the cell. The Rayleigh scattering signal is calibrated by varying the pressure in the cell at room temperature in the range of $P = 50$–500 Torr. The effects of ionization, electronic excitation, and dissociation on the Rayleigh scattering cross section are neglected because this group of particles makes up a small fraction (<1%) of the bulk of the gas, and since the measurements take place after the discharge burst, not within the plasma.

3. Kinetic model

The quasi-zero-dimensional kinetic model used to interpret the experimental results is developed using the same approach as described in [22]. The model solves the electron energy equation (a moment of the Boltzmann equation), the heavy species energy equation, and the equations for the species concentrations in the plasma and afterglow. It incorporates the electron impact ionization of Ar and O_2,

$$e^- + Ar \rightarrow Ar^+ + e^- + e^-, \quad (3)$$

$$e^- + O_2 \rightarrow O_2^+ + e^- + e^-, \quad (4)$$

electronic and vibrational excitation,

$$e^- + Ar \rightarrow Ar^* + e^-, \quad (5)$$

$$e^- + O_2 \rightarrow O_2(v) + e^-. \quad (6)$$

O_2 dissociation,

$$e^- + O_2 \rightarrow O + O + e^-, \quad (7)$$

state-specific vibrational relaxation of O_2 by O_2 and O, including multi-quantum vibration–translation (V–T) relaxation by O atoms,

$$O_2(v) + O \leftrightarrow O_2(v - \Delta v) + O, \ \Delta v = 1 - 30, \quad (8)$$

and vibration–vibration (V–V) energy transfer,

$$O_2(v) + O_2(w) \leftrightarrow O_2(v-1) + O_2(w+1); \quad (9)$$

quenching of excited metastable Ar atoms resulting in O_2 dissociation,

$$Ar^* + O_2 \leftrightarrow Ar + O + O; \quad (10)$$

and chemical reactions among O, O_2, and O_3,

$$O + O + M \leftrightarrow O_2(v) + M, \quad (11)$$

$$O + O_2 + M \leftrightarrow O_3 + M, \quad (12)$$

$$O + O_3 \leftrightarrow O_2(v) + O_2(w). \quad (13)$$

Additional processes, listed in the supplemental information, include the ion conversion (e.g. to O_4^+ and Ar_2^+), electron-ion recombination, electron attachment to O_2 and detachment from O^- and O_2^- ions, and ion-ion neutralization.

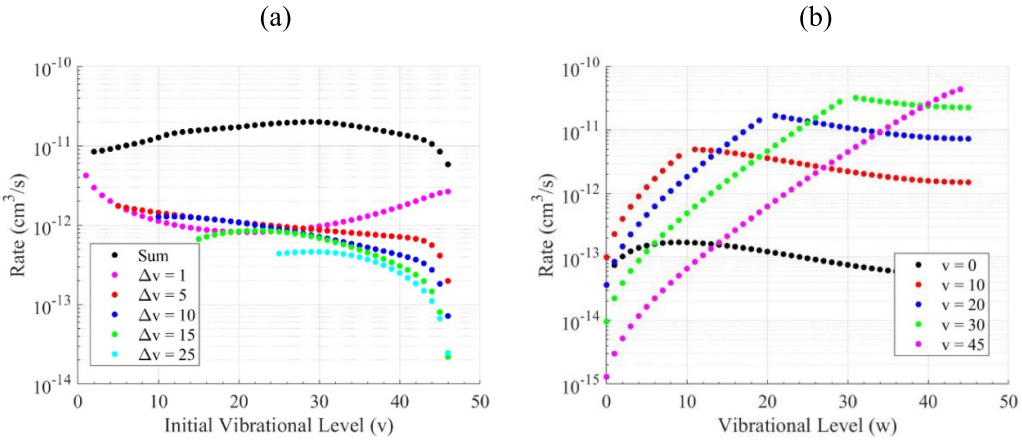

Figure 6. (a) State-specific V–T relaxation rates of O_2 by O atoms, equation (8), plotted vs. initial O_2 vibrational level at $T = 600$ K; (b) State-specific O_2–O_2 V–V exchange rates, equation (9), plotted vs. vibrational level v at $T = 600$ K.

These processes do not have a significant effect on the peak electron density during the ns discharge pulses, which is controlled by electron impact ionization and charge separation, resulting in rapid plasma self-shielding [23]. They control the electron density decay on a much longer time scale, between the discharge pulses. As discussed in our previous work [24], the detailed kinetics of the electron density decay in the discharge afterglow are of relatively minor importance. Basically, peak electron density is weakly sensitive to the low residual electron density before the pulses. Therefore, the accurate prediction of the electron density decay and of the ion composition between the discharge pulses is not critical.

In the present experiment the plasma is also generated in the heated ambient air outside of the reactor. Because of this, the ns pulse discharge power coupled into the plasma in the flow channel is treated as an adjustable parameter, varied to match the temperature rise measured at the end of the discharge burst. The electron impact rate coefficients are predicted by the Boltzmann equation solver BOLSIG [25] with the cross sections taken from [26, 27], the results are tabulated vs. electron temperature (T_e), and used as inputs in the model. The state-specific V–T coefficients, as well as the state-specific rates of dissociation and recombination for O_2–O are predicted by the quasiclassical trajectory calculations, including the multi-quantum transitions [5, 28]. The state-to-state V–T and V–V rate coefficients, as well as the state-specific rates of dissociation and recombination for O_2–O_2, predicted by the semiclassical trajectory calculations [29], are interpolated [30] and rescaled [5] to account for the accurate O_2 vibrational energy spacing, $v = 0$–46. V–T relaxation of O_2 by Ar is neglected, since at these relatively low temperatures it is much slower compared to that of O_2–O and O_2–O_2 [28, 31]. The state-specific V–T rates for O_2–O and V–V rates for O_2–O_2 at $T = 600$ K are plotted in figure 6. The state-specific rates of O atom recombination generating the vibrationally excited $O_2(v)$ molecules, reaction of equation (11) with M = O, predicted by quasiclassical trajectory calculations [28], are plotted in figure 7 for $T = 600$ K. The

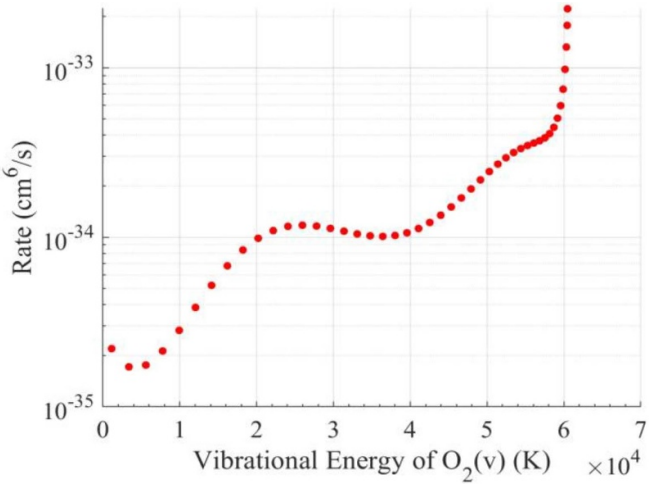

Figure 7. State-specific O atom recombination rate coefficients, equation (11), plotted vs. vibrational energy of the $O_2(v)$ product, at $T = 600$ K.

recombination reaction predominantly generates highly vibrationally excited molecules, near the dissociation limit. From the detailed balance, this indicates O_2 vibrational excitation significantly enhances the dissociation rates.

At the present conditions, the recombination reactions of equations (12) and (13) are expected to contribute substantially to the O_2 vibrational excitation, since the net rate of O + O_2 + M reaction is significantly higher compared to that of the O + O + M reaction. To the best of our knowledge, the theoretical predictions for the state-specific rates of this reaction are not available. In the present work, the reaction of equation (12) is assumed to be non-state-specific, since the populations of O_2 ($v > 0$) are much lower than the ground state population. The state-specific rates of the bimolecular reaction of equation (13), $k(\rightarrow v, \rightarrow w)$, are parametrized in terms of a single adjustable parameter, using the approach developed by Treanor and Marrone [32, 33]. The Treanor-Marrone reaction rate model was developed to quantify the effect of

vibrational excitation on the rate of dissociation of diatomic molecules, as follows,

$$k(v\rightarrow,T)=C\cdot\exp\left(-\frac{D-E_v}{T_u}\right), \tag{14}$$

where $k(v\rightarrow,T)$ is the state-specific dissociation rate coefficient from the vibrational level v, D is the dissociation energy, E_v is the vibrational energy,

$$\frac{1}{T_u}=\frac{1}{T}+\frac{1}{U}, \tag{15}$$

and the parameter U was varied over the range of $0<U<\infty$. In equation (14), C is found from the net dissociation rate at thermal equilibrium, $k(T)=\sum_v k(v\rightarrow,T)f_{\rm eq}(v,T)$. At $U=\infty$, the model is vibrationally 'non-preferential' [32], such that the contribution of all vibrational levels to dissociation in thermal equilibrium is the same. It can be shown that this is equivalent to the translational and vibrational energies being equally effective in overcoming the dissociation barrier. As shown in [34], this assumption has no basis in collision dynamics, due to the momentum conservation, which makes the vibrational mode energy more effective. The non-preferential model is also at variance with the experimental results. For any $0<U<\infty$, the contribution of highly excited vibrational states to dissociation is more significant compared to that of the lower vibrational levels (i.e. the reaction is vibrationally preferential). From the detailed balance, this also indicates that the state-specific rates of the reverse reaction, i.e. recombination to vibrationally excited states, $k(\rightarrow v,T)$, increase with vibrational energy, qualitatively similar to the state-specific rates of O + O recombination plotted in figure 7. Setting $U<0$ would correspond to the vibrationally 'anti-preferential' model, when the state-specific dissociation and recombination rates decrease with the vibrational energy.

In the present work, we adopt the same approach to the state specific rates of the reaction of equation (13), as follows:

$$k(v\rightarrow,w\rightarrow)=C\cdot\exp\left(-\frac{E_a-(E_v+E_w)}{T_u}\right), \tag{16}$$

where E_a is the activation energy, E_v and E_w are the vibrational energies of O_2 molecules,

$$\frac{1}{T_u}=\frac{1}{T}+\frac{1}{U}. \tag{17}$$

As before, the value of C in equation (16) is found from matching the net reaction rate at thermal equilibrium, $k(T)=\sum_{v,w}k(v\rightarrow,w\rightarrow)f_{\rm eq}(v,T)f_{\rm eq}(w,T)$. The reverse rate coefficients are calculated from the detailed balance,

$$k(\rightarrow v,\rightarrow w)\left(n_{O_3}n_O\right)_{\rm eq}=k(v\rightarrow,w\rightarrow)\left(n_{O_2(v)}n_{O_2(w)}\right)_{\rm eq}, \tag{18}$$

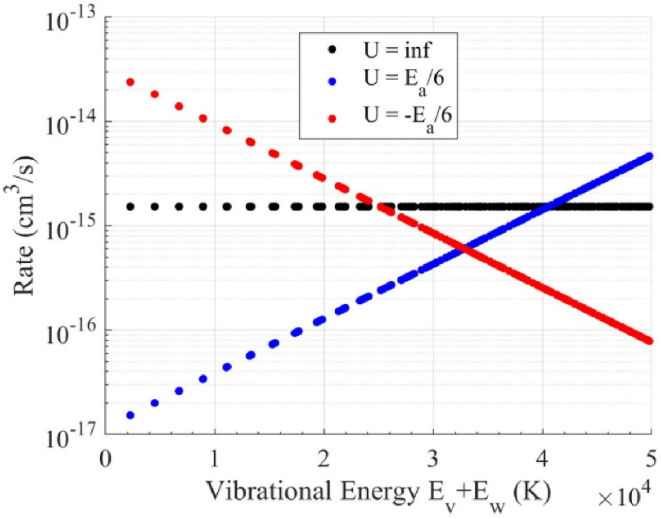

Figure 8. State-specific rate coefficients of reaction of equation (13) at $T=600$ K, plotted vs. total vibrational energy of O_2 products (E_v+E_w), predicted by the generalized Treanor-Marrone model using different assumptions: $U=\infty$ (non-preferential), $U=E_a/6$ (vibrationally preferential), and $U=-E_a/6$ (vibrationally anti-preferential).

or

$$k(\rightarrow v,\rightarrow w)\exp\left(-\frac{E_v+E_w}{T}\right)=k(v\rightarrow,w\rightarrow)$$
$$\frac{Z_{O_3}(T)Z_O(T)}{Z^2_{O_2}(T)}\exp\left(-\frac{\Delta E}{T}\right)=k(v\rightarrow,w\rightarrow)K_P(T). \tag{19}$$

In equation (19), $Z_i(T)$ are the partition functions of species i, ΔE is the reaction energy, and $K_P(T)$ is the equilibrium constant. Again, the value of the adjustable parameter U quantifies how effectively the vibrational energies of O_2 molecules contribute towards overcoming the activation energy of the reaction generating O and O_3, as well as the vibrational distribution of O_2 molecules in the reverse reaction. This assumes that the state-specific reaction rate coefficients depend on the total available vibrational energy, rather than on the specific values of the vibrational energies of two reactant molecules summing to the same total value.

Figure 8 plots the state-specific reaction rates for three different assumptions, $U=\infty$ (non-preferential), $U>0$ (preferential to high vibrational levels), and $U<0$ (preferential to low vibrational levels), respectively. In all three cases, the state-specific rates are normalized to the net rate at thermal equilibrium. In the absence of the high-fidelity theory predictions for the state-specific reaction rates for a 4-atom reaction, this approach enables a qualitative assessment of the O_2 vibrational distribution during the dominant recombination reaction of equation (13). Varying the value of the parameter U also makes possible quantifying the sensitivity of the experimental data

and modeling predictions to the $O_2(v)$ distribution generated by this reaction.

The effect of diffusion and convective cooling of the flow is taken into account using a quasi-zero-dimensional corrections, based on the flow channel height and length of the electrodes, as was done in our previous work using the same approach as in [22]. For a rectangular cross section flow channel, the diffusion time is $\tau_{\text{diff}} = [D(\frac{\pi}{h})^2]^{-1}$, where D is the diffusion coefficient and h is the channel height. The flow residence time between the electrodes is $\tau_{res} = \frac{1}{2}\frac{V}{\dot{V}}$, where V is plasma volume, $\dot{V}$ is the volumetric flow rate, and the factor 1/2 accounts for the flow non-uniformity (assuming the fully developed flow in the channel).

4. Results and discussion

Figure 9 plots the ns pulse discharge voltage waveform in a 20% O_2–Ar mixture, at a pressure of $P = 200$ Torr and temperature of $T = 600$ K. The voltage waveform taken at room temperature, with the flow channel filled with 1 atm of ambient air, is plotted for comparison. As mentioned in section 2, the current and energy coupled to the plasma in the flow reactor have not been measured, since the plasma is also generated outside of the flow channel (see discussion of figure 10 below). At these conditions, current and voltage measurements would yield only the total power dissipated in the plasma, both inside and outside the channel. In the kinetic model, the coupled power waveform is assumed to be Gaussian, with the same rise time as the pulse voltage waveform, and the total pulse energy coupled to the plasma adjusted to match the measured temperature rise in the plasma. This assumption is justified by the previous measurements and modeling predictions of the power coupled to ns pulse discharges in the plane-to-plane geometry [35]. The discharge power waveform used in the model is also plotted in figure 9. The coupled pulse energy used in the model varies from 1.76 mJ/pulse at $T = 400$ K to 1.32 mJ/pulse at $T = 600$ K, and 1.06 mJ/pulse at $T = 800$ K. The coupled pulse energy used in the present work is consistent with our previous measurements in nitrogen at $P = 150$–250 Torr and room temperature, using a pulse generator with similar output pulse parameters [36]. As expected, the measured coupled pulse energy is reduced as the temperature is increased, consistent with the kinetic modeling predictions [35].

The entire set of the experimental data in the present work is obtained in a 20% O_2–Ar mixture at the same pressure, $P = 200$ Torr, and temperatures of $T = 400$–800 K. Single-shot, broadband plasma emission images at temperatures of $T = 400$ K, 600 K, and 800 K are shown in figure 10. At all operating conditions, after the first pulse in the burst, the plasma becomes diffuse for the rest of the discharge burst. The surface streamers visible in the images at $T = 600$ K and 800 K originate at the electrode surfaces exposed to the heated ambient air in the furnace and are formed on the outside surface of the flow channel. They do not affect the uniformity of the plasma in the reactor, although the plasma generation outside of the channel makes the evaluation of the coupled pulse energy more challenging.

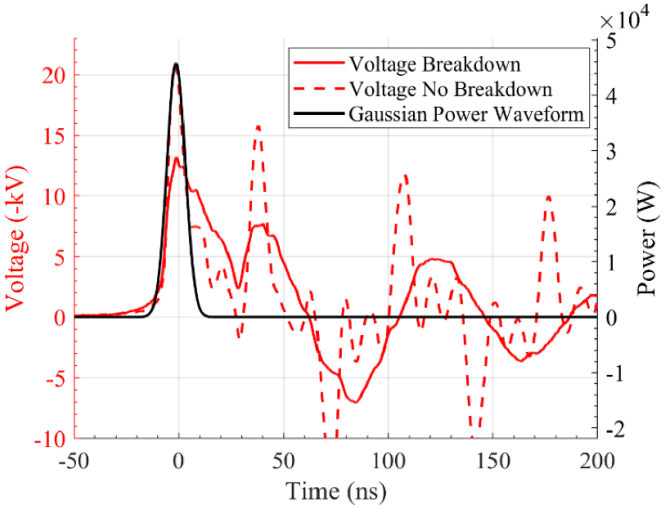

Figure 9. Ns pulse discharge voltage waveform, plotted together with the coupled power waveform used in the kinetic model. 20% O_2–Ar, $T = 600$ K, $P = 200$ Torr, pulse #100 in the burst. The voltage waveform measured when the reactor channel is filled with ambient air at 1 atm and $T = 300$ K (No Breakdown) is shown for comparison.

The electron density predicted by the kinetic is plotted in figure 11. The modeling predictions are shown for pulse #199 in a 200-pulse burst, at the furnace temperature of $T = 400$ K. The initial electron density before the pulse is the residual ionization from the previous pulse, generated 10 μs earlier. During the pulse, the electron density increases by several orders of magnitude, reaching $n_e \approx 10^{12}$ cm^{-3} (see figure 11(a)). On this short time scale, ≈10 ns, ionization by electron impact is the dominant plasma kinetic process, limited only by the rapid charge separation in the plasma and shielding of the applied electric field [23]. This is the main process that limits the energy coupled to the plasma. In comparison, the ion conversion, electron-ion recombination, electron attachment, and ion-ion neutralization processes occur on much longer time scales (several μs), and do not affect the electron density during the discharge pulse. Therefore, the energy coupled to the plasma during the discharge pulses is controlled only by the rate coefficient of electron impact ionization, specifically its dependence on the electron temperature, predicted by solving the electron energy balance equation.

The electron density between the pulses decreases on the time scale of ∼1 μs, due to the 3-body electron attachment to O_2 molecules,

$$e^- + O_2 + M \leftrightarrow O_2^- + M, \tag{20}$$

and electron-ion dissociative recombination, e.g.

$$e^- + O_2^+ \rightarrow O + O, \tag{21}$$

$$e^- + Ar_2^+ \rightarrow Ar + Ar. \tag{22}$$

At the present conditions, the attachment dominates the plasma decay between the pulses, although as the temperature increases, the reverse thermal detachment from O_2^- ions becomes more pronounced. As discussed in section 3, the

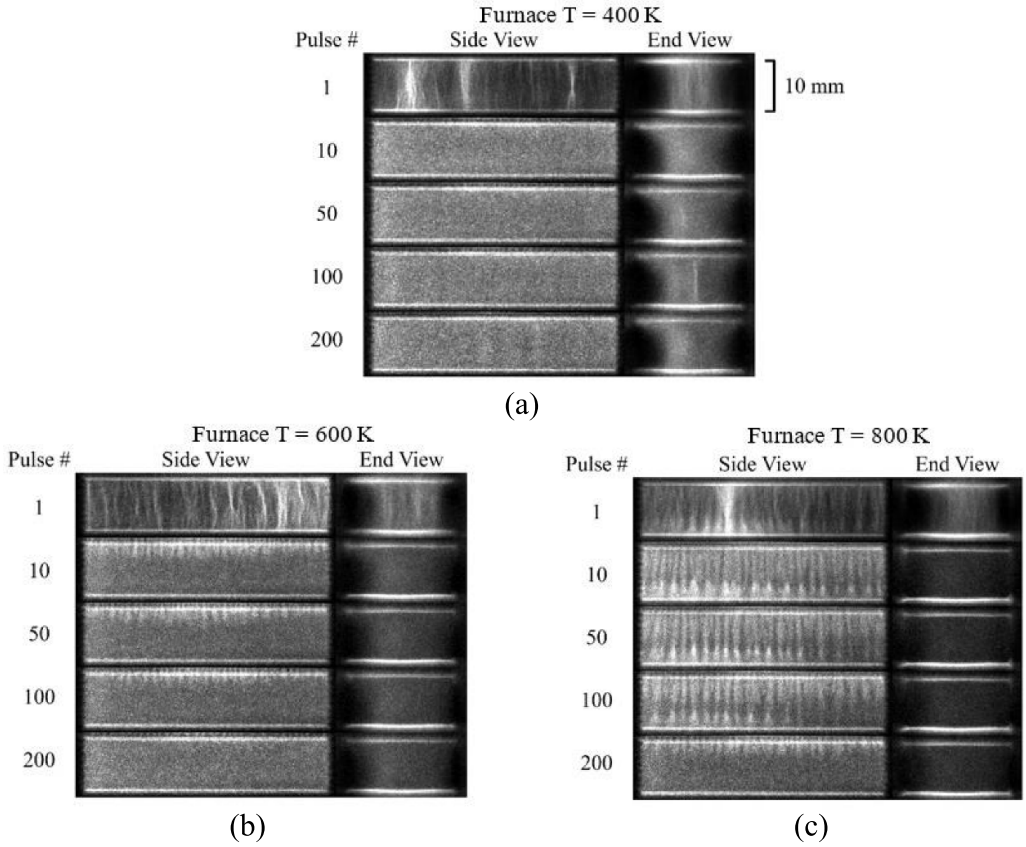

Figure 10. Single-shot, broadband plasma emission images during a 200-pulse discharge burst, at different furnace temperatures, (a) $T = 400$ K, (b) $T = 600$ K, and (c) $T = 800$ K. 20% O_2–Ar, $P = 200$ Torr, pulses #1–200 in the burst, camera gate 5 μs.

detailed kinetics of the electron density decay between the pulses is of relatively little importance, since (a) no energy is coupled to the plasma in the afterglow, and (b) the peak electron density during the discharge pulse is weakly sensitive to the residual electron density before the pulse, as long as it remains low, i.e. $n_e(t < 0) \ll n_e(t > 0)$ [35]. This makes the modeling predictions essentially insensitive to the rates of electron decay processes.

Figure 12 shows the time-resolved temperature measurements in the flow reactor by Rayleigh scattering thermometry, and figure 13 compares the modeling predictions for the temperature with the experimental data. From figures 12 and 13, it can be seen that the discharge burst heats the flow by up to 80–100 K above the baseline flow temperature, and the temperature remains nearly constant for approximately 10 ms after the discharge burst. After this, the temperature in the region between the electrodes is gradually decreasing to the baseline value, due to the convective cooling of the flow (see figure 13). Since the temperature variation during the discharge burst is relatively modest, the coupled pulse energy is assumed to remain the same during the entire burst. From figure 13, it is apparent that the kinetic modeling predictions for the time resolved temperature are in good agreement with the Rayleigh scattering thermometry data. As discussed above, this agreement was achieved by adjusting the pulse coupled energy value in the heavy species energy equation included in the kinetic model, to match the peak temperature rise during the burst. The temperature decay in the afterglow is controlled by the convective cooling of the flow.

Preheating the flow is essential for reducing the effect of ozone chemistry on the O atom recombination kinetics, due to reactions of equations (12) and (13). By increasing the temperature, the thermal decomposition of ozone, i.e. the reverse reaction of equation (12), is enhanced, such that the contribution of both reactions to the net rate of O atom recombination is somewhat reduced. However, at the present experimental conditions, the effect of ozone chemistry remains the dominant recombination process. Diminishing it would require reducing the O_2 fraction in the mixture, such that the O atom number density after the discharge burst would exceed significantly that of O_2. At these conditions, the detection of $O_2(v)$ molecules becomes difficult due to their considerably lower number densities.

Time-resolved, absolute O atom number densities measured by ps TALIF in the preheated 20% O_2–Ar mixture, after the excitation by a 200-pulse discharge burst, are plotted in figure 14. It can be seen that the peak O atom number densities at these conditions are comparable, and that their decay after the burst slows down as the temperature is increased. As expected, heating the mixture results in a more rapid thermal decomposition of ozone, such that the O atom decay due to the reactions of equations (12) and (13) becomes less significant. Also, the rate of O atom recombination in the reaction of equation (11) decreases with temperature, due to the

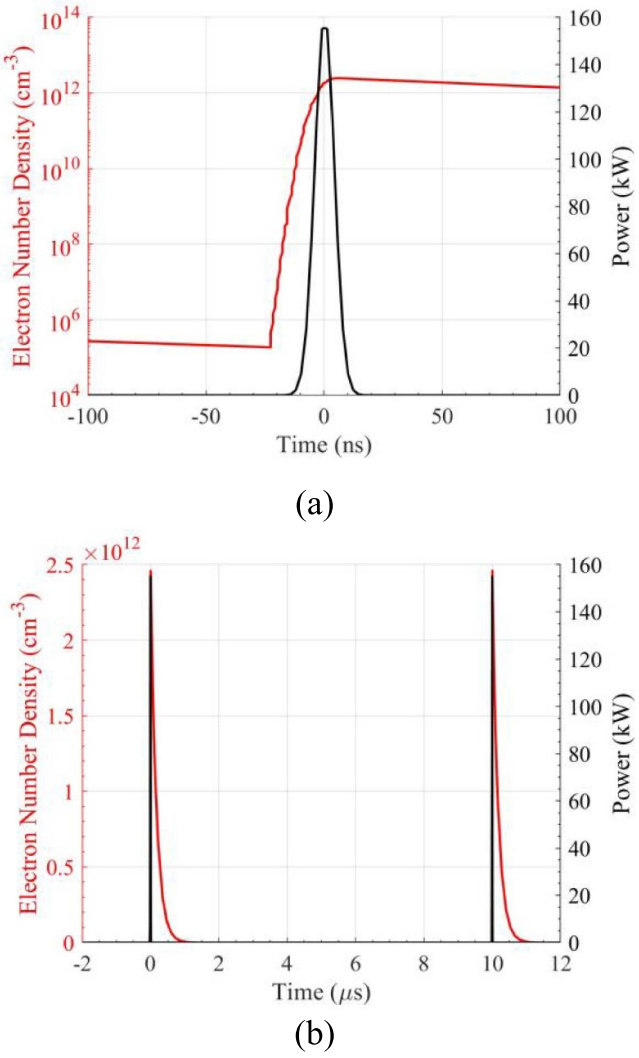

Figure 11. Predicted electron density during (a) and after (b) pulse #199 at the furnace temperature of $T = 400$ K.

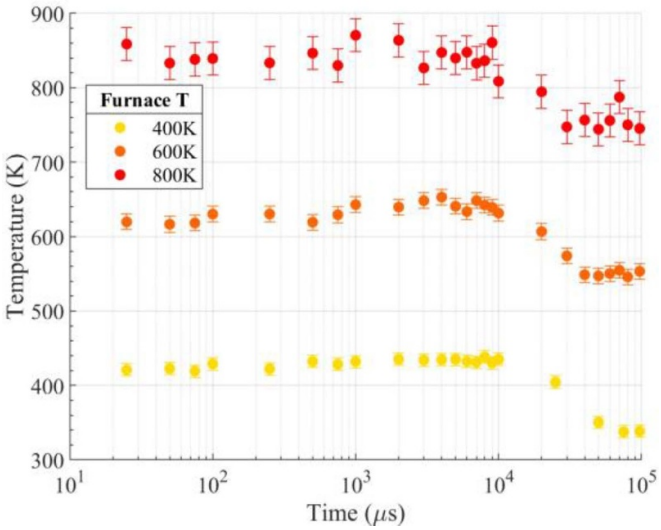

Figure 12. Rayleigh scattering thermometry measurements made using the 355 nm beam from the pump Nd:YAG laser. The flow is heated in the discharge by up to 80–100 K above the furnace temperature. The effect of convective cooling by the flow after $t = 10$ ms is evident.

negative temperature dependence of the recombination rate coefficient and the lower total number density of O atoms at elevated temperatures. The number density of O atoms measured by TALIF is overpredicted by the model by approximately a factor of 2, which may be due to several reasons. First, the TALIF calibration depends on the ratio of Xe and O atom absorption cross sections. The absorption cross sections of these two photon transitions have been measured in multiple experiments, yielding substantially varying results [21, 37], indicating a significant source of uncertainty. Second, the picosecond laser/OPO system used in the present experiment had significant shot-to-shot variation of the output pulse energy, beam profile, and spectral line shape. Finally, the predictive capability of the kinetic model at the present conditions is limited by the two-term approximation for the electron energy distribution function used by BOLSIG, which predicted the quasi-steady state electron impact rate coefficients (specifically rates of ionization, dissociation of O_2, and electronic excitation of Ar) vs. electron temperature. The two-term approximation remains accurate up to the reduced electric field of $E/N \sim 10^{-15}$ V·cm^2 = 100 Td [38], while the peak E/N at the present conditions is $(E/N)_{\text{peak}} \approx 500$ Td, varying on the time scale of ~10 ns (see figure 9).

To assess the effect of ozone generation at the present conditions, figure 15 plots the time resolved ozone number density inferred from the UV absorption measurements at 250 nm, at the furnace temperatures of $T = 400$ K and 600 K. At $T = 800$ K, absorption by ozone is below the detection limit. In these measurements, the absorption path during and immediately after the discharge burst is assumed to be equal to that of the discharge electrodes (plasma length), and the 'baseline' ozone number density in the flow before the burst is subtracted from the absorption signal. This is justified, since the estimated flow residence time between the electrodes, based on the plasma volume and the volumetric flow rate, is approximately $\tau_{\text{res}} = 30$ ms, much longer compared to the discharge burst duration, $\tau_{\text{burst}} = 2$ ms. Also, subtraction of the 'baseline' ozone number density accumulated in the plasma flow reactor downstream of the electrodes as a result of multiple discharge bursts (before the most recent burst), removes the uncertainty of the absorption path occurring on the long time scale.

From figure 15, it is readily apparent that the ozone number density inferred from the absorption measurements is much lower compared with the kinetic modeling predictions, by up to a factor of ~40 at $T = 400$ K and a factor of ~4 at $T = 600$ K. We are confident that this difference is much higher compared to the uncertainty in the net rate coefficients of the dominant chemical reactions controlling the ozone number density, equations (11)–(13). The rates of these reactions used in the present work are consistent with those in [39, 40], which are in good agreement with the ozone concentration measurements at steady state conditions. The most likely reason for

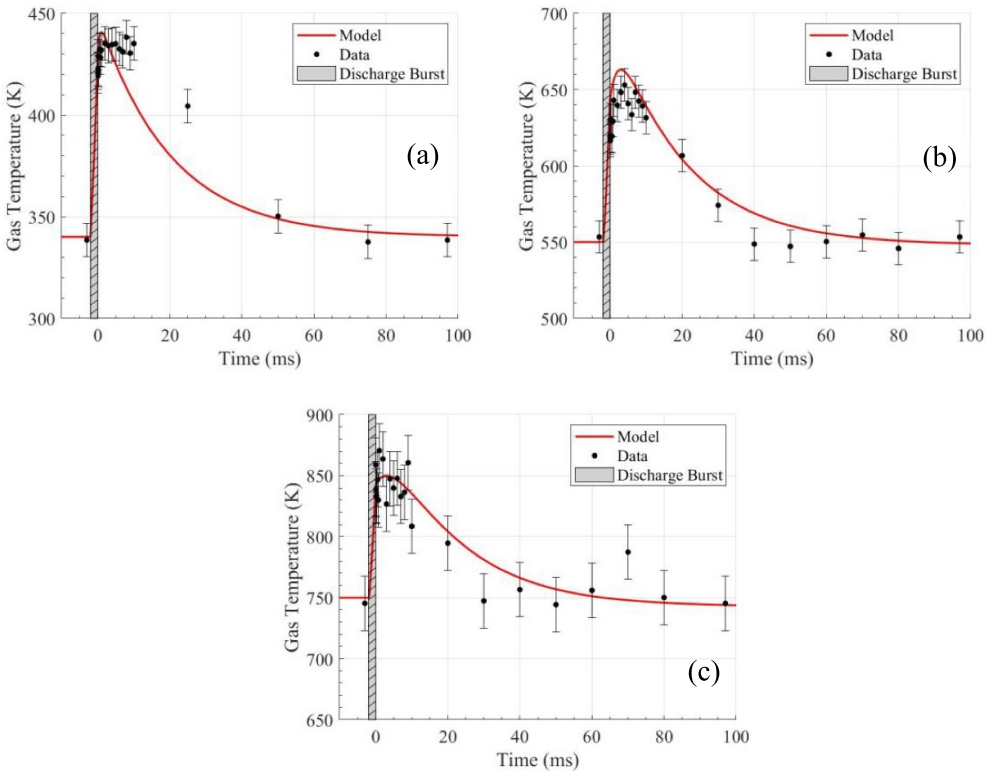

Figure 13. Comparison of the modeling predictions for the temperature in the plasma with the experimental data from Rayleigh scattering thermometry, for three different furnace temperatures, (a) $T = 400$ K, (b) $T = 600$ K, and (c) $T = 800$ K. The coupled pulse energy in the model is adjusted to match the peak measured temperature.

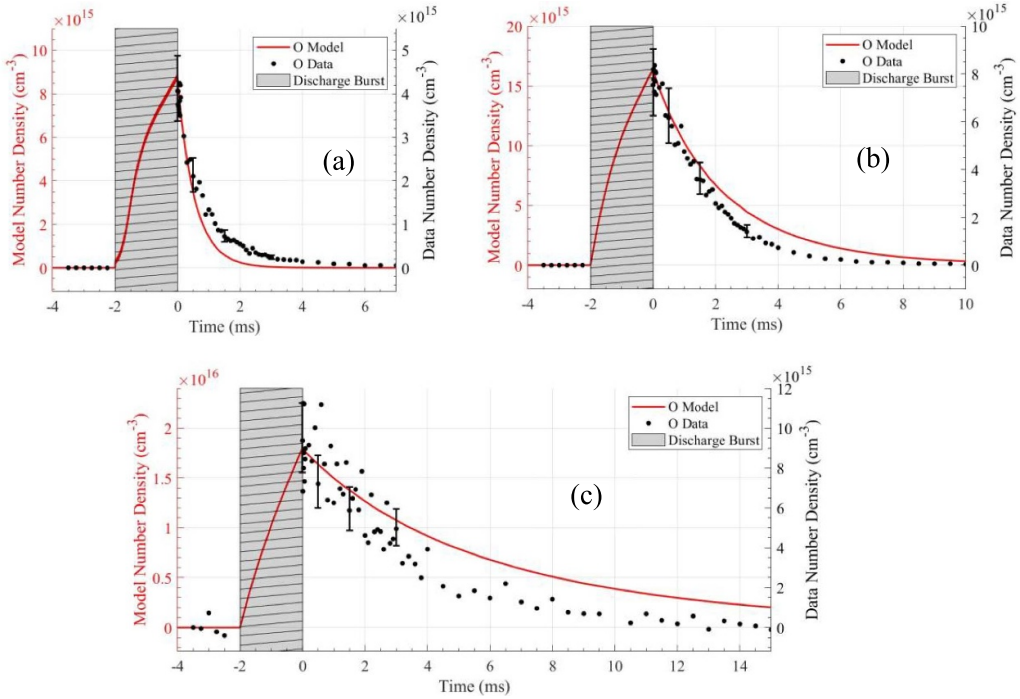

Figure 14. Time-resolved, absolute O atom number densities in the heated 20% O_2–Ar mixture at different furnace temperatures, (a) 400 K, (b) 600 K, (c) 800 K, plotted vs. delay time after the excitation by the discharge burst and compared with the modeling predictions.

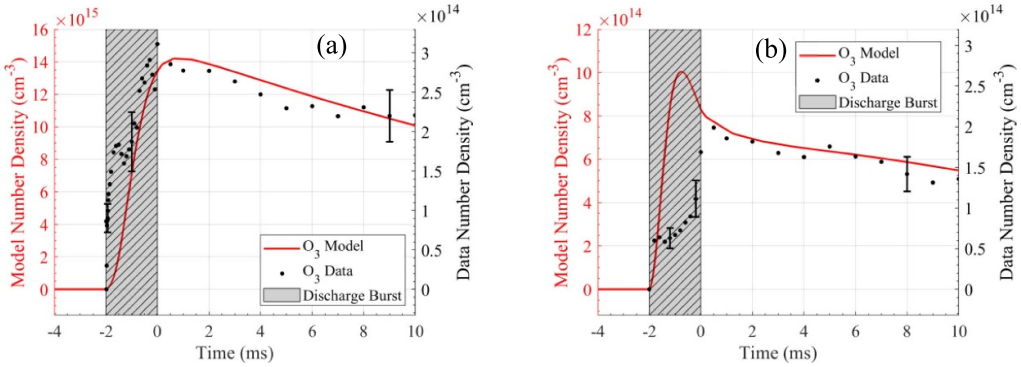

Figure 15. Time-resolved, absolute ozone number density in 20% O_2–Ar mixture at furnace temperatures of $T = 400$ K (a) and 600 K (b), plotted vs. delay time after the excitation by the discharge burst and compared with the modeling predictions. Note the use of two different axes for the experimental data (right) and modeling predictions (left).

the discrepancy observed in the present measurements is the collimation, focusing, and alignment of the UV lamp output, which are challenging to achieve in a flow channel over 1 m long and 10 mm height, without clipping the channel walls. This may result in a portion of the output bypassing the plasma, which does not fill the channel completely (see figure 10). Therefore, the ozone number density inferred from the UV absorption is interpreted as relative data. Both from the relative ozone measurements and the modeling predictions (see figure 15), the ozone number density after the discharge burst (at $t = 0$–10 ms), remains nearly the same, varying only by ∼20%–30%. This is due to the relatively slow recombination of O_2 with O atoms, equation (12), balanced by the $O_3 + O$ reaction, equation (13). Thus, the ozone number density on this time scale remains in quasi-equilibrium. Most importantly, this indicates that the effect of the photolytic dissociation of ozone by the laser pulses is negligible at the present conditions, since the measured $O_2(v)$ LIF signal, discussed in detail below, follows the O atom number density over the entire range of temperatures and vibrational quantum numbers. Indeed, if the photolytic effect were significant, the LIF signal would follow the ozone number density and remain nearly steady in time.

The time-resolved relative populations of O_2 vibrational levels measured in the discharge afterglow at $T = 400$, 600, and 800 K and normalized by their values at the end of the discharge burst (at $t = 5$ μs) are plotted in figures 16–18. They are compared with the relative populations predicted by the kinetic model, $f_v = \frac{[O_2(v)]}{[O_2]}$, normalized in the same way. The data are shown for all accessible vibrational levels, $v = 8$–11, 13, and 17–21 and plotted vs. delay time after the discharge burst. At $v = 12$, the LIF signal is affected by the strong emission from the plasma, generated with and without oxygen in the mixture. The measured O_2(v) relative populations are compared with the modeling predictions, which include the dominant processes of O_2 vibrational excitation and decay. This comparison provides insight into the kinetics of O_2(v) decay in the afterglow.

From figure 16, showing the data for $T = 400$ K, it is evident that the $O_2(v)$ populations before the discharge burst are below the detection limit. During the discharge pulses, O_2 vibrational levels, up to $v = 42$, are populated by electron impact excitation, equation (6). In the beginning of the burst (during first ∼10–20 pulses), the vibrational level populations increase rapidly in time (see figures 16–18). Later in the burst, their rise becomes slower or followed by the decay, mainly due to the rapid multi-quantum V–T relaxation by O atoms, generated by electron impact dissociation of O_2 and by quenching of metastable Ar atoms, equations (7) and (10). The 'downward' V–V relaxation in collisions with the non-excited O_2 in the ground vibrational state,

$$O_2(v) + O_2(w = 0) \leftrightarrow O_2(v - 1) + O_2(w = 1), \qquad (23)$$

also contributes to this process. The time scale for the V–T relaxation at the present conditions, estimated based on the rate coefficients predicted in [28]. (see figure 6) and the measured O atom number density, is $\tau_{VT} \sim 10$ μs, comparable to the time interval between the discharge pulses, 10 μs. The estimated characteristic time for the V–V exchange, based on the V–V rates for O_2–O_2 measured in [20], is similar, $\tau_{VV} \sim 10$ μs. Therefore, detecting the vibrationally excited molecules on a significantly longer time scale after the discharge burst indicates the additional O_2 vibrational excitation, generated during the O atom recombination, equation (11), and recombination with ozone, equation (13).

In the present work, the O_2 vibrational populations are monitored after the discharge burst excitation for time delays ranging from 4 μs to over 5 ms, i.e. significantly longer compared to the characteristic time for the V–V and V–T relaxation. The initial rapid decay of $O_2(v)$ molecules excited during the discharge, due to the V–T relaxation by O atoms and downward V–V exchange on the time scale of ∼10 μs, is readily apparent, for all three temperatures studied. This decay is also reproduced by the kinetic model (see figures 16–18). The comparison of the modeling prediction with the experimental data demonstrates the critical importance of the multi-quantum V–T relaxation of $O_2(v)$ by O atoms (see the state-specific rates plotted in figure 6). They contribute significantly into the overall relaxation rates and including the processes with $\Delta v = 5$–10 has a noticeable effect on the modeling predictions (see figure 6(a)).

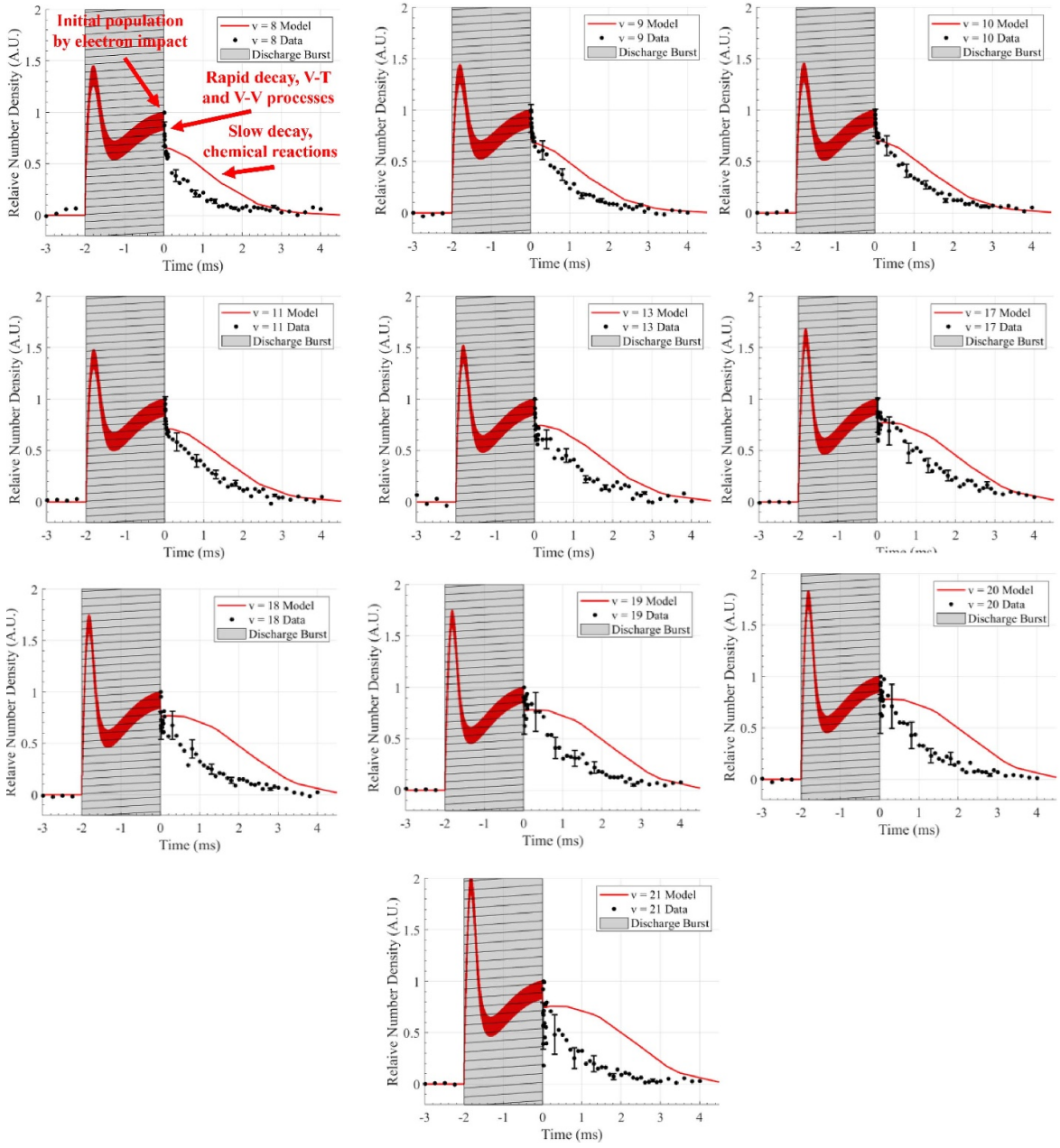

Figure 16. Time-resolved, relative $O_2(v)$ number densities in 20% O_2–Ar mixture at a furnace temperature of $T = 400$ K for all accessible vibrational levels, plotted vs. delay time after the discharge burst and compared with modeling predictions. The rapid initial decay, caused primarily by V–T relaxation, $O_2(v) + O \leftrightarrow O_2(v—\Delta v) + O$, followed by the slow decay controlled by the $O_3 + O \leftrightarrow O_2(v) + O_2(w)$ chemical reaction, is readily apparent. The vibrational levels are labeled in the plot legends.

On a ms time scale, the $O_2(v)$ decay slows down considerably, indicating an additional source of $O_2(v)$ generation after the discharge burst is over. Since the characteristic time scales for the electron-ion recombination, electron attachment, ion-ion recombination, and quenching of the excited electronic states of Ar are much shorter, this source is attributed to the reactions of the neutral species, initiated by the O atom recombination, i.e. the reactions of equations (11)–(13). The decay time of $O_2(v)$ molecules in figures 16–18, approximately 2–6 ms, is significantly shorter compared to the excited flow residence time between the electrodes, $\tau_{res} \sim 30$ ms at $T = 600$ K. Again, the kinetic modeling predictions reproduce the evolution of $O_2(v)$ after the burst rather well (see figures 16–18). The sudden transition from the rapid decay due to the V–T relaxation by O atoms, equation (8) and downward O_2–O_2 V–V exchange, equation (23), to the much slower decay driven by the O atom recombination, resulting in a well-pronounced 'kink' in figures 16–18, is readily apparent. The $O_2(v)$ populations predicted by the model on the ms time scale are not affected by the initial (nascent) vibrational populations generated by electron impact during the last discharge pulse. The predicted $O_2(v)$ decay time becomes

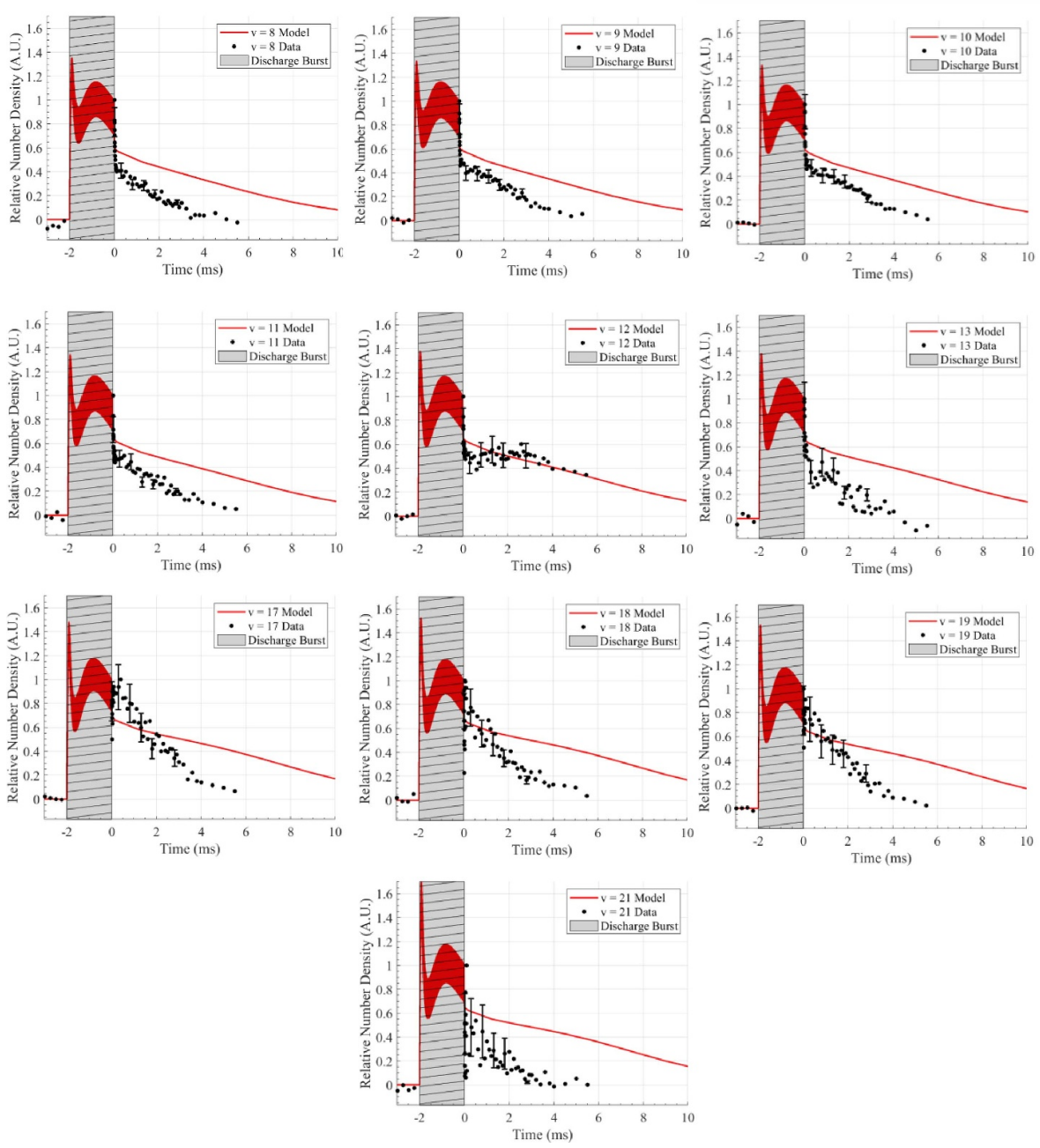

Figure 17. Time-resolved, relative $O_2(v)$ number densities in 20% O_2–Ar mixture at a furnace temperature of $T = 600$ K for all accessible vibrational levels, plotted vs. delay time after the discharge burst and compared with modeling predictions. The vibrational levels are labeled in the plot legends.

longer as the temperature increases. The analysis of the reaction pathways shows that this is due to the reduction of the ozone number density at higher temperatures (see figure 15), when the relatively slow reaction of equation (11) makes a more significant contribution to the net O atom recombination rate.

The experimental data and modeling predictions for each vibrational level, plotted in figures 16–18, are consistent with each other. In all cases, the initial rapid decay of $O_2(v)$ due to the V–T and V–V relaxation, followed by the slow decay controlled by the chemical reactions, is clearly evident. However, it becomes less pronounced for the higher vibrational levels, and at lower temperatures. For all cases shown in figures 16–18, heating the mixture results in the lower vibrational level populations during the long-term decay after the discharge burst. Also, the modeling predictions for the entire range of the relative $O_2(v)$ populations appear very similar, indicating that the kinetics of their decay is governed by the same processes.

It should be noted that the rates of all kinetic processes controlling the O_2 vibrational populations after the discharge burst are linear in $O_2(v)$. This is true even for the V–V exchange, since it is dominated by the collision of $O_2(v)$ with the O_2 molecules in the ground vibrational state, see equation (23). At the present conditions, the relative populations of the excited

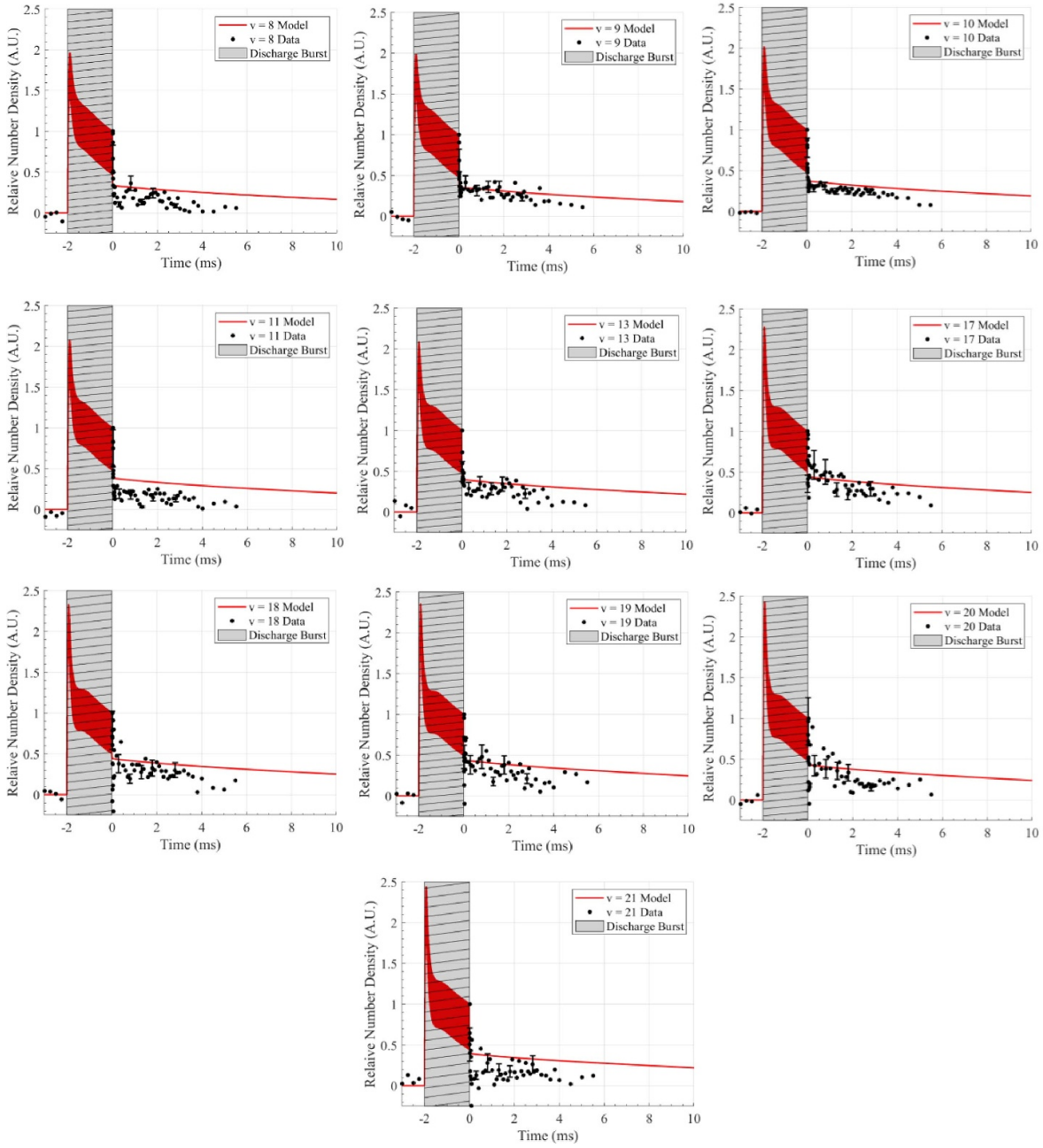

Figure 18. Time-resolved, relative $O_2(v)$ number densities in 20% O_2–Ar mixture at a furnace temperature of $T = 800$ K for all accessible vibrational levels, plotted vs. delay time after the discharge burst and compared with modeling predictions. The vibrational levels are labeled in the plot legends.

vibrational levels are all much lower than 1, i.e. $\frac{[O_2(w>0)]}{[O_2]} \ll 1$. This is caused by the rapid O_2–O V–T relaxation between the discharge pulses, such that the vibrationally excited molecules do not accumulate during the discharge burst. This is readily apparent from figures 16–18, where the predicted $O_2(v)$ populations during the discharge burst (at $-2 \leqslant t \leqslant 0$ ms) reach a quasi-steady-state. Therefore, the modeling predictions are not sensitive to the absolute $O_2(v)$ populations. The key parameters controlling the absolute $O_2(v)$ populations in the afterglow are the number densities of O atoms and ozone.

Figure 19 plots the distribution of absolute O_2 vibrational level populations in a 20% O_2–Ar mixture at different furnace temperatures, at $t = 0$ ms (i.e. right after the end of the discharge burst). It can be seen that the vibrational levels ranging from $v = 5$ to $v = 20$ are populated, creating an extended 'plateau' in the O_2 vibrational distribution function. As discussed previously, vibrational levels $v = 14$–16 are not accessible to the present LIF diagnostics. The agreement between the experimental populations and the modeling predictions, also plotted in figure 19, is rather poor. The absolute O_2 populations inferred from the LIF measurements are only as

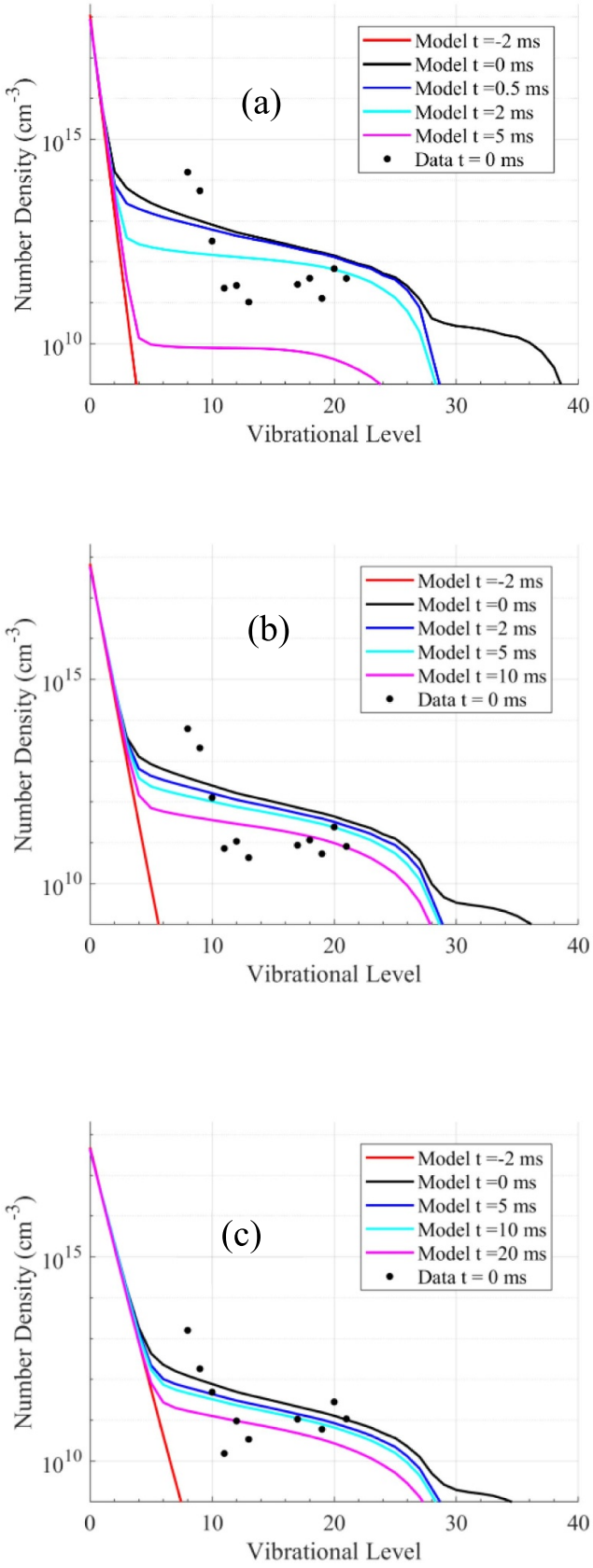

Figure 19. Predicted vibrational distribution functions for the furnace temperatures of $T = 400$ K (a), $T = 600$ K (b), and $T = 800$ K (c), compared with the absolute $O_2(v)$ number densities measured at the end of the discharge burst (at $t = 0$ ms). At $t = -2$ ms, the distribution functions are at equilibrium with the flow translational temperature.

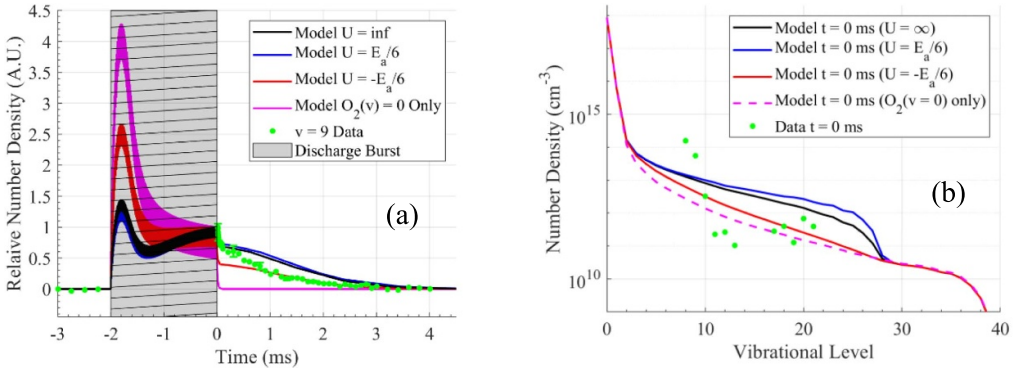

Figure 20. (a) Time-resolved, relative $O_2(v = 9)$ populations at the furnace temperature of $T = 400$ K, compared with the modeling predictions, for different models of $O + O_2$ recombination reaction, non-preferential ($U = \infty$), vibrationally preferential ($U = E_a/6$), anti-preferential ($U = -E_a/6$), and no vibrational excitation in reaction products. (b) Measured and predicted absolute $O_2(v)$ vibrational distributions at the end of the discharge burst (at $t = 0$ ms), for the same model assumptions.

accurate as the calibration technique used in the experimental data reduction, which is sensitive to the spectral line shape of the OPO output measured by a relatively low-resolution spectrometer. The other critical factor controlling the accuracy of the absolute calibration is the rate of predissociation of the upper LIF state, $O_2(B,v' = 0)$, which dominates its decay rate as well as the fluorescence yield [17]. The use of a higher fidelity spectroscopic model, which includes both bound–bound and bound-free pump transitions, such as developed more recently [41, 42], may well improve the calibration accuracy.

From figure 19, it can be seen that on the ms time scale after the discharge burst, the plateau in the O_2 vibrational distribution function, predicted by the kinetic model and extending over $v \sim 5$–30, decays in a self-similar fashion, essentially preserving its shape. Analysis of the modeling predictions indicates that this behavior is due to the rapid V–T relaxation of $O_2(v)$ by O atoms, for which the rates of the single-quantum and multi-quantum jumps are comparable. The modeling predictions are less sensitive to the distribution of the state-specific rates of reactions of equations (11) and (13), since their net rates are much slower compared to that of the V–T relaxation, which rapidly redistributes the O_2 populations over the vibrational energy manifold.

The effect of the state-specific rate coefficients of reaction of equation (13), $O_3 + O \leftrightarrow O_2(v) + O_2(w)$, which controls the net rate of $O_2(v,w)$ generation in the afterglow, on the vibrational distribution function is illustrated in figure 20. Figure 20(a) compares the measured relative population of $O_2(v = 9)$ with the modeling predictions at $T = 400$ K, for three different values of parameter U used in the calculations of the state-specific reaction rates in equations (16)–(19), plotted in figure 8 ($U = \infty$, $+E_a/6$, and $-E_a/6$). The choice of $U = \pm E_a/6$ is similar to the value used in the Treanor-Marrone model of preferential dissociation [33] (used for the $O_2 + M \leftrightarrow O + O + M$ reaction), which yields best overall agreement with the shock tube dissociation measurements. As illustrated in figure 20(a), the predictions of the non-preferential ($U = \infty$) and vibrationally preferential ($U = + E_a/6$) reaction rate models are close to each other and in better agreement with the measured relative $O_2(v)$ populations. On the other hand, the vibrationally anti-preferential model ($U = -E_a/6$) predicts a more rapid $O_2(v)$ decay rate, compared to the experimental observations. Finally, the modeling predictions assuming that O_2 molecules produced by the $O_3 + O$ reaction are formed in the vibrational ground state, $v = w = 0$, are at variance with the experimental data. In this case, the relatively slow O_2(v) decay scale disappears, providing definitive evidence that the reaction of equation (13) controls the O_2 vibrational relaxation after the discharge burst. Clearly, (i) this reaction dominates the $O_2(v)$ populations in the afterglow, and (ii) its products are formed in the predominantly vibrationally excited states. Without a state-specific ozone conversion pathway present, the reaction of equation (11) would dominate the O atom recombination. However, at the present conditions the contribution of this reaction remains insignificant, such that its contribution cannot be isolated with confidence.

The O_2 vibrational distribution function predicted by the model is compared with the measured absolute $O_2(v)$ populations in figure 20(b), using the same modeling assumptions. The shape of the predicted distribution function is similar in all three cases; however, for the non-preferential ($U = \infty$) and vibrationally preferential ($U = + E_a/6$) cases, the vibrationally excited plateau is higher and exhibits a sudden drop above vibrational level $v \sim 27$, which corresponds to the reverse (dissociation) reaction activation energy. At this point the rate of reaction of equation (13) is reduced dramatically, resulting in the 'kink' in the VDF. This drop is not pronounced for the vibrationally anti-preferential case ($U = -E_a/6$), because the near-threshold recombination rates in this case are very low (see figure 8).

As stated above, the modeling predictions in figures 13–20 are made for the discharge input power (coupled pulse energy) adjusted to match the measured temperature rise at the end of the burst (see figure 13), which is the most accurately measured parameter in the present work. To assess the sensitivity of the modeling predictions to the discharge input power, additional calculations were made with the coupled energy per pulse reduced by a factor of 2, to match the measured

O atom number density. As expected, in this case the model underpredicts the temperature rise during the discharge burst. However, the dominant trends in the time-resolved populations of vibrationally excited O_2 remain largely unchanged, although the absolute populations also decrease by about a factor of 2.

5. Summary

Dissociation of an O_2–Ar mixture by a burst of ns discharge pulses in a heated flow reactor is used to study the kinetics of O_2 vibrational excitation during the O atom recombination. Time-resolved vibrational level populations of the ground electronic state molecular oxygen, $O_2(v = 8–20)$ in the partially dissociated, recombining 20% O_2–Ar mixture, preheated up to $T = 400–800$ K, are measured by ps Laser Induced Fluorescence on the O_2 Schumann-Runge bands, with absolute calibration by NO LIF. Time-resolved, absolute O atom number density in the O_2–Ar mixture dissociated by the discharge burst is measured by ps Two-Photon absorption LIF (TALIF) with Xe calibration. The time-resolved gas temperature in the reactor is measured by Rayleigh scattering thermometry. Time-resolved ozone number density in the heated flow reactor is measured by broadband UV absorption. The ozone absorption measurements are treated as relative data, due to the challenges in the alignment of the UV lamp output through the long flow channel, which may result in a portion of the transmitted light bypassing the plasma. The relative ozone measurements are critical for the demonstration that the measured $O_2(v)$ and O number densities are not affected by the photodissociation of ozone. This is apparent since the ozone absorption signal remains approximately the same on a ms time scale after the discharge burst (within ∼20%–30%), while both $O_2(v)$ LIF and TALIF signals decay nearly completely within ∼1–3 ms.

The results indicate a rapid initial decay of the $O_2(v = 8–20)$ populations generated by electron impact in the discharge, on a ∼10 μs time scale, due to the V–T relaxation by O atoms and O_2–O_2 V–V exchange. This decay is followed by a much slower reduction, on the time scale of several ms, due to the additional generation of $O_2(v)$ in the chemical reactions initiated by the O atom recombination. Both these trends are reproduced by the kinetic modeling predictions, incorporating the state-specific processes of O_2 vibrational excitation by electron impact, vibrational–translational (V–T) relaxation, vibrational-vibrational (V–V) exchange, and recombination reactions. The modeling predictions are compared with the experimental data after matching the temperature rise and decay during and after the discharge burst, respectively, which is used as the most accurate comparison metric.

Comparison with the modeling predictions demonstrates clearly that the O atom number density decay and the $O_2(v)$ population decay after the discharge burst, on a ms time scale, is controlled by the generation of vibrationally excited molecules in a chemical reaction $O + O_3 \leftrightarrow O_2(v) + O_2(w)$. This occurs even at higher temperatures, up to at least $T = 800$ K. Although the ozone number density at elevated temperatures is reduced significantly, this reaction still dominates the O atom recombination reaction, $O + O + M \leftrightarrow O_2(v) + M$, since O_2 is only partially dissociated in the plasma, such that the rate of $O + O_2 + M$ recombination is more significant. Thus, the quasi-steady-state $O_2(v)$ populations in the afterglow are controlled by the balance between the $O + O_2$ recombination reactions (generation) and the multiquantum V–T relaxation by O atoms (decay). The present results indicate that the $O + O_3$ recombination reaction generates highly vibrationally excited O_2 molecules, and that this reaction dominates the $O_2(v)$ populations in the afterglow.

The modeling predictions are not very sensitive to the dependence of the state-specific rates of the $O + O_3$ recombination reactions on the vibrational energy of the products, since the rapid multiquantum V–T relaxation 'smears' the nascent $O_2(v)$ distribution produced by this reaction. However, the overall agreement with the data is better for the $O_2(v)$ generation rates preferential toward the high vibrational levels of O_2. The agreement between the absolute $O_2(v)$ populations measured in the experiment and predicted by the model is rather poor, likely due to the limited accuracy of the O_2 LIF calibration, specifically the measurements of the spectral line shape and center wavelength of the OPA output. The predictive capability of the LIF data reduction model would also benefit significantly from the development of a more advanced and accurate spectroscopic model predicting the cross sections of both bound–bound and bound-free absorption transitions in the O_2 Shumann-Runge bands. However, since the dominant kinetic processes controlling the population of O_2 vibrational levels in the afterglow are linear in $[O_2(v)]$, the modeling predictions for the relative populations are not sensitive to their absolute values.

At the present conditions, the vibrationally excited O_2 is predominantly generated by a chemical reaction between O atoms and ozone. The detection of vibrationally excited O_2 formed during the direct recombination of O atoms needs additional data taken in preheated mixtures with low O_2 mole fraction, below ∼1%, at the conditions when the discharge excitation would result in dissociation of most of O_2 molecules in the mixture. The sensitivity of the present LIF diagnostic may improve significantly using a fs laser system with a spectrally broad output. This would provide access to multiple pump transitions during the same laser pulse and enhance the LIF signal at the same $O_2(X,v)$ number density, thereby improving the detection limit. The present work is the first experimental and modeling study of O_2 vibrational kinetics in a recombining O_2–O mixture. It demonstrates the capability for the measurements of time-resolved, absolute populations of vibrationally excited O_2, up to at least $v = 20$, as well as the O atom number density. It also demonstrates the quantitative insight into the processes controlling the $O_2(v)$ populations in the recombining gas mixture, with the exception of $O + O_3$ reaction, for which the high-fidelity state-specific theory predictions are not available.

Further work needs to focus on the experimental conditions when nearly all molecular oxygen is dissociated, prior to the laser diagnostic measurements. This would largely exclude the effect of ozone formation and subsequent ozone reactions,

such that the effect of O + O + M ↔ $O_2(v)$ + M reaction can be isolated. The main significance of the present work is the development of the experimental platform, as well as the diagnostic and modeling tools for the analysis of the energy partition in the O atom recombination reaction.

Data availability statement

All data that support the findings of this study are included within the article (and any supplementary files).

ORCID iDs

Keegan Orr https://orcid.org/0000-0003-3677-8976
Fabrizio Esposito https://orcid.org/0000-0003-0586-5866
Iole Armenise https://orcid.org/0000-0002-9440-0026
I V Adamovich https://orcid.org/0000-0001-6311-3940

References

[1] Park C 1990 *Nonequilibrium Hypersonic Aerodynamics* (Wiley) ch 3
[2] Ibraguimova L B, Sergievskaya A L, Levashov V Y, Shatalov O P, Tunik Y V and Zabelinskii I E 2013 Investigation of oxygen dissociation and vibrational relaxation at temperatures 4000–10800 K *J. Chem. Phys.* **139** 034317
[3] Streicher J W, Krish A, Hanson R K, Hanquist K M, Chaudhry R S and Boyd I D 2020 Shock-tube measurements of coupled vibration–dissociation time-histories and rate parameters in oxygen and argon mixtures from 5000 K to 10 000 K *Phys. Fluids* **32** 076103
[4] Streicher J W, Krish A and Hanson R K 2021 Coupled vibration-dissociation time-histories and rate measurements in shock-heated, nondilute O_2 and O_2-Ar mixtures from 6000 to 14 000 K *Phys. Fluids* **33** 056107
[5] Armenise I and Esposito F 2012 Dissociation-recombination models in hypersonic boundary layer O_2/O flows *Chem. Phys.* **398** 104
[6] Pan T-J, Wilson T J and Stephani K A 2019 Vibrational state-specific model for dissociation and recombination of the $O_2(^3\Sigma_g^-)$ + O(^{3}P) system in DSMC *J. Chem. Phys.* **150** 074305
[7] Kondur C and Stephani K A 2022 Rate constants and molecular recombination pathways of oxygen from quasi-classical trajectory simulations of the O_3 system *Chem. Phys.* **552** 111357
[8] Geistfeld E C, Torres E and Schwartzentruber T 2023 Quasi-classical trajectory analysis of three-body collision induced recombination in neutral nitrogen and oxygen *J. Chem. Phys.* **159** 154111
[9] Andrienko D A Recombination of oxygen in the vicinity of a silica surface *AIAA Paper 2024–0223, AIAA SciTech 2024 Forum* (*Orlando, FL, 8–12 January 2024*)
[10] Gudmundsson J T and Thorsteinsson E G 2007 Oxygen discharges diluted with argon: dissociation processes *Plasma Sources Sci. Technol.* **16** 399
[11] Corr C S, Gomez S and Graham W G 2012 Discharge kinetics of inductively coupled oxygen plasmas: experiment and model *Plasma Sources Sci. Technol.* **21** 055024
[12] Annušová A, Marinov D, Booth J-P, Sirse N, da Silva2 M L, Lopez B and Guerra V 2018 Kinetics of highly vibrationally excited O_2(X) molecules in inductively coupled oxygen plasmas *Plasma Sources Sci. Technol.* **27** 045006
[13] Winters C, Eckert Z, Yin Z, Frederickson K and Adamovich I V 2018 Measurements and kinetic modeling of atomic species in fuel-oxidizer mixtures excited by a repetitive nanosecond pulse discharge *J. Phys. D: Appl. Phys.* **51** 015202
[14] van den Bekerom D C, Jans E, Yang X, Paul A C, Andrienko D and Adamovich I V Measurements of vibrationally excited oxygen produced in recombining O-O_2-Ar mixtures *AIAA Paper 2021–1145, AIAA SciTech 2021 Forum* (*Orlando, FL, January 2021*) pp 11–21
[15] Molina L T and Molina M J 1986 Absolute absorption cross sections of ozone in the 185- to 350-nm wavelength range *J. Geophys. Res.* **91** 14501
[16] Astholr D C, Croce A E and Troe J 1982 Temperature dependence of the ozone absorption coefficient in the hartley continuum *J. Phys. Chem.* **86** 696
[17] Lee M P and Hanson R K 1986 Calculations of O_2 absorption and fluorescence at elevated temperatures for a broadband argon fluoride laser source at 193 nm *J. Quant. Spectrosc. Radiat. Transfer* **36** 425
[18] Settersten T B, Patterson B D and Gray J A 2006 Temperature- and species dependent quenching of NO $A^2\Sigma^+(v'=0)$ probed by two-photon laser-induced fluorescence using a picosecond laser *J. Chem. Phys.* **124** 234308
[19] Luque J and Crosley D R 1999 LIFBASE: database and spectral simulation program (version 2.1.1) *SRI International Report MP-99-009*
[20] Park H and Slanger T G 1994 O_2(X, v = 8–22) 300 K quenching rate coefficients for O_2 and N_2, and O_2(X) vibrational distribution from 248 nm O_3 photodissociation *J. Chem. Phys.* **100** 287
[21] Niemi K, Schulz-von der Gathen V and Döbele H F 2001 Absolute calibration of atomic density measurements by laser-induced fluorescence spectroscopy with two-photon excitation *J. Phys. D: Appl. Phys.* **34** 2330
[22] Richards C, Jans E, Gulko I, Orr K and Adamovich I V 2022 N_2 vibrational excitation in atmospheric pressure ns pulse and RF plasma jets *Plasma Sources Sci. Technol.* **31** 034001
[23] Orr K, Yang X, Gulko I and Adamovich I V 2020 Formation and propagation of ionization waves during Ns pulse breakdown in plane-to-plane geometry *Plasma Sources Sci. Technol.* **29** 125022
[24] Telfah H, Jans E, Raskar S and Adamovich I V 2022 Kinetics of HO_2 radical formation and decay in Ns pulse O_2-He plasmas over a liquid water surface *Plasma Sources Sci. Technol.* **31** 115019
[25] Hagelaar G J M and Pitchford L C 2005 Solving the Boltzmann equation to obtain electron transport coefficients and rate coefficients for fluid models *Plasma Sources Sci. Technol.* **14** 722
[26] Itikawa Y 2009 Cross sections for electron collisions with oxygen molecules *J. Phys. Chem. Ref. Data* **38** 1
[27] Laporta V, Celiberto R and Tennyson J 2013 Resonant vibrational-excitation cross sections and rate constants for low-energy electron scattering by molecular oxygen *Plasma Sources Sci. Technol.* **22** 025001
[28] Esposito F, Armenise I, Capitta G and Capitelli M 2008 O-O_2 state-to-state vibrational relaxation and dissociation rates based on quasiclassical calculations *Chem. Phys.* **351** 91
[29] Billing G D and Kolesnick R E 1992 Vibrational relaxation of oxygen. State to state rate constants *Chem. Phys. Lett.* **200** 382
[30] Capitelli M, Armenise I and Gorse C 1997 State-to-state approach in the kinetics of air components under re-entry conditions *J. Thermophys. Heat Transfer* **11** 570
[31] Kim J G and Boyd I D 2015 Thermochemical nonequilibrium analysis of O_2 +Ar based on state-resolved kinetics *Chem. Phys.* **446** 76

[32] Treanor C E and Marrone P V 1962 Effect of dissociation on the rate of vibrational relaxation *Phys. Fluids* **5** 1022
[33] Marrone P V and Treanor C E 1963 Chemical relaxation with preferential dissociation from excited vibrational levels *Phys. Fluids* **6** 1215
[34] Macheret S O and Rich J W 1993 Nonequilibrium dissociation rates behind strong shock waves: classical model *Chem. Phys.* **174** 25
[35] Takashima K, Yin Z and Adamovich I V 2013 Measurements and kinetic modeling of energy coupling in volume and surface nanosecond pulse discharges *Plasma Sources Sci. Technol.* **22** 015013
[36] Jans E R, Raskar S, Yang X and Adamovich I V 2021 Kinetics of metastable $N_2(A^3\Sigma_u^+, v)$ molecules in high-pressure nonequilibrium plasmas *Plasma Sources Sci. Technol.* **30** 025003
[37] Drag C, Marmuse F and Blondel C 2021 Measurement of the two-photon excitation cross-section of the $6p'[3/2]_2$ and $6p'[1/2]_0$ levels of Xe I at the wavelengths 224.3 and 222.6 nm *Plasma Sources Sci. Technol.* **30** 075026
[38] Raizer Y P 1991 *Gas Discharge Physics* (Springer)
[39] Zhao H, Yang X and Ju Y 2016 Kinetic studies of ozone assisted low temperature oxidation of dimethyl ether in a flow reactor using molecular-beam mass spectrometry *Combust. Flame* **173** 187
[40] Bang S, Snoeckx R and Cha M S 2023 Temperature–dependent kinetics of ozone production in oxygen discharges *Plasma Chem. Plasma Process.* **43** 1453
[41] Bykova N G and Kuznetsova L A 2008 Study of the absorption characteristics of molecular oxygen in the Schumann-Runge system at high temperatures: I. Calculations of absorption spectra *Opt. Spectrosc.* **105** 668
[42] Bykova N G, Zabelinskii I E, Ibraguimova L B and Shatalov O P 2008 Study of the absorption characteristics of molecular oxygen in the Schumann-Runge system at high temperatures: II. Experiment and comparison with calculation *Opt. Spectrosc.* **105** 674